

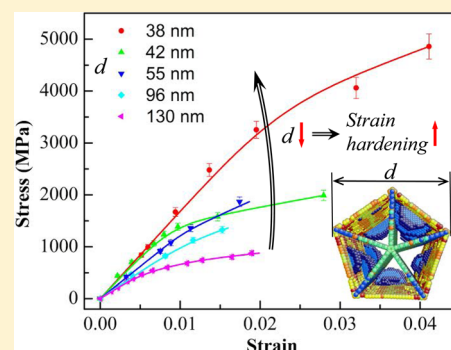
Strain Hardening and Size Effect in Five-fold Twinned Ag Nanowires

Sankar Narayanan,[†] Guangming Cheng,[‡] Zhi Zeng,[†] Yong Zhu,^{*,‡} and Ting Zhu^{*,†,§}[†]Woodruff School of Mechanical Engineering, Georgia Institute of Technology, Atlanta, Georgia 30332, United States[‡]Department of Mechanical and Aerospace Engineering, North Carolina State University, Raleigh, North Carolina 27695, United States[§]School of Materials Science and Engineering, Georgia Institute of Technology, Atlanta, Georgia 30332, United States

Supporting Information

ABSTRACT: Metallic nanowires usually exhibit ultrahigh strength but low tensile ductility owing to their limited strain hardening capability. Here we study the unique strain hardening behavior of the five-fold twinned Ag nanowires by nanomechanical testing and atomistic modeling. In situ tensile tests within a scanning electron microscope revealed strong strain hardening behavior of the five-fold twinned Ag nanowires. Molecular dynamics simulations showed that such strain hardening was critically controlled by twin boundaries and pre-existing defects. Strain hardening was size dependent; thinner nanowires achieved more hardening and higher ductility. The size-dependent strain hardening was found to be caused by the obstruction of surface-nucleated dislocations by twin boundaries. Our work provides mechanistic insights into enhancing the tensile ductility of metallic nanostructures by engineering the internal interfaces and defects.

KEYWORDS: Nanowire, twin boundary, strain hardening, size effects, in situ experiment, molecular dynamics



Nanoscale structures like nanowires are known to exhibit ultrahigh yield strength but limited hardening and low ductility (tensile strain to fracture).^{1–5} Insufficient hardening can severely affect the mechanical integrity of the constituent nanostructures in nanomechanical devices and other technological applications. This lack of hardening has been understood to be primarily due to the absence of effective obstacles within the nanowire, which otherwise could block the movement of crystalline defects like dislocations so as to produce macroscopic hardening.³ Hence engineering the internal interfaces and defects of the nanoscale materials toward improving hardening has been a significant area of research in recent years.^{4,5}

Many recent studies have focused on single-crystalline metallic nanowires through experiments and modeling. Single crystalline nanowires of face-centered cubic (fcc) metals like silver, nickel, copper and gold (Figure 1a) have been found to deform via dislocation-mediated plasticity^{6–11} or via deformation twinning and lattice reorientation^{12–16} without exhibiting pronounced hardening. To promote strain hardening, nanowires with coherent internal twin boundaries (TBs) have recently received much attention, owing to the capability of the TBs to contribute to hardening by acting as barriers to dislocation motion. For example, nanowires with horizontal TBs (Figure 1b) have been studied.^{17–23} But effective hardening due to these horizontal TBs requires uniformly small twin spacing across the entire length of the nanowires, thus imposing a challenge to nanowire synthesis. In addition, the inclined TBs in nanowires (Figure 1c) are subjected to nonzero resolved shear stress during axial loading of nanowires

and are thus prone to migrate, causing twin coarsening.²² In contrast, nanowires with vertical TBs (Figure 1d) have shown promising results specifically with respect to strain hardening. Zhu et al.²⁴ reported pronounced strain hardening in Ag nanowires (AgNWs) with a well-defined five-fold vertical twin structure. Filleter et al.²⁵ further studied this type of AgNWs of various diameters and found that the smaller diameter AgNWs exhibited stronger strain hardening than the larger ones. Despite these promising results, the mechanisms underlying the strain hardening and associated size effects in nanowires with vertical TBs remain unclear.

Recently, several groups have conducted molecular dynamics (MD) simulations to explore the mechanical properties and deformation behavior of the five-fold twinned AgNWs.^{25–31} However, these MD works were unable to capture the hardening behavior in the stress–strain responses, which has been observed in experiments. Hence questions as to why MD simulations cannot complement the experimental results or explain the mechanisms governing the hardening behavior, remain unanswered.

In this work, we report a combined experimental and modeling study that combines in situ tensile testing within a scanning electron microscope (SEM) and large scale MD simulations for the five-fold twinned AgNWs. We were able to capture the strain hardening behavior of these nanowires in both experiments and modeling. The detailed hardening

Received: March 14, 2015

Revised: May 6, 2015

Published: May 12, 2015

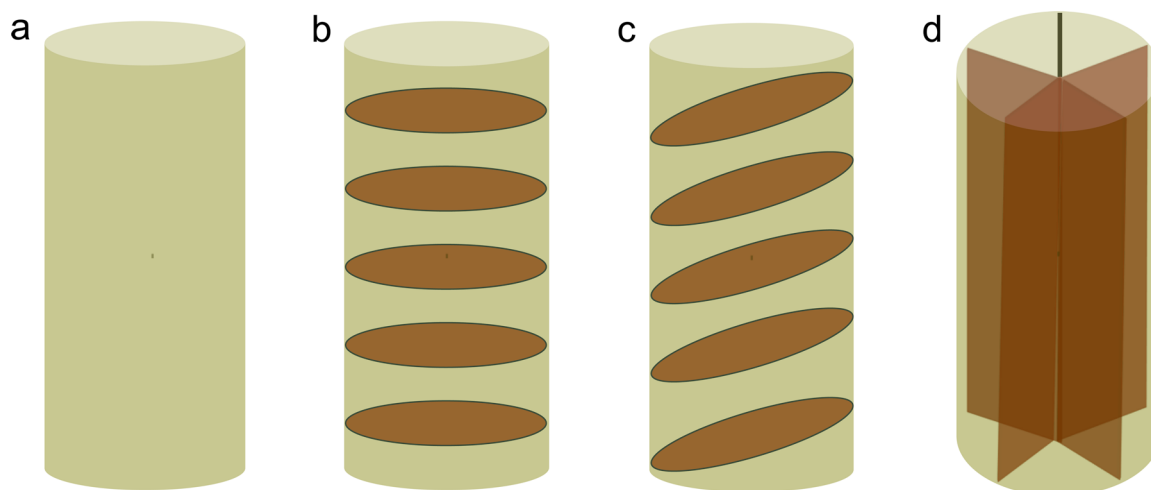


Figure 1. Schematics of metal nanowires with different types of ordered arrangement of TBs, colored in brown. (a) Single crystal nanowire without TBs. (b) Nanowire with horizontal TBs. (c) Nanowire with inclined TBs. (d) Nanowire with five-fold vertical TBs.

mechanisms were further revealed by analyses of MD results. The hardening behavior was shown to be critically dependent on the nanowire diameter, as well as the pre-existing defects. The simulated necking and fracture modes are compared with experiments. These results provide insights into enhancing the tensile ductility of metallic nanostructures by engineering the internal interfaces and defects.

Results and Discussion. Five-fold twinned AgNWs were synthesized by a modified polyol process.^{32,33} Figure 2 panels a and b respectively show the transmission electron microscopy (TEM) cross-sectional and perspective images of a five-fold AgNW. Tensile tests were conducted for the AgNWs with diameters ranging from 38 to 130 nm within a scanning electron microscope (SEM) (see Methods). The measured stress–strain curves are plotted in Figure 2c. Interestingly, AgNWs of smaller diameters can harden more than larger ones. The smallest wire of 38 nm in diameter hardens and achieves an ultimate tensile strength of 4.8 GPa, while the largest wire of 130 nm in diameter shows limited hardening. These results are in close agreement to the experimental results by Filletter et al.²⁵

The strain hardening behavior was quantified by fitting the measured stress–strain data to the Ramberg–Osgood relationship, which is commonly used for materials exhibiting a smooth elastic–plastic transition. That is, the stress–strain curve is described as a continuous function with three parameters, such that the total strain is given by

$$\varepsilon = \frac{\sigma}{E} + \left(\frac{\sigma}{H} \right)^{1/n} \quad (1)$$

where ε is strain, σ is stress, E is Young's modulus, and H and n are constants. The first term on the right side of eq 1, σ/E , is the elastic part of the strain, while the second term, $(\sigma/H)^{1/n}$, accounts for the plastic part; the parameters H and n characterize the strain hardening behavior of the material.

Table 1 lists the fitting parameters of E , H , and n based on eq 1 for the experimental stress–strain data of five-fold twinned Ag NWs with different diameters; the associated fitting stress–strain curves are plotted in Figure 2c. The work hardening exponent, n , decreases from 0.23 to 0.14 as the NW diameter decreases from 130 to 38 nm, while Young's modulus, E , increases from 96 to 169 GPa correspondingly. The size

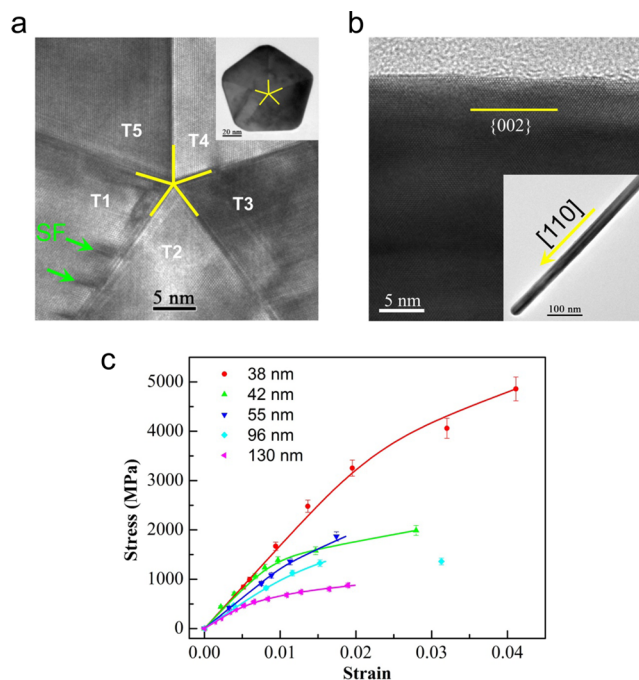


Figure 2. Experimental results of the five-fold twinned AgNW. (a) High-resolution TEM image of the nanowire cross section showing twin variants of T1–T5. Pre-existing defects (i.e., partials and stacking faults) are observed close to the TBs. Inset shows the pentagonal shape of the cross section. (b) High-resolution TEM image of the nanowire showing the atomically rough surface, indicative of the presence of surface defects such as steps. Inset shows the overall morphology of the nanowire. (c) Measured stress–strain data (symbols) for Ag NWs of various diameters with the Ramberg–Osgood fitting curves (solid lines) based on eq 1.

dependence of Young's modulus is consistent with the previous work.^{24,25}

The unique hardening behavior and its size dependence in five-fold twinned AgNWs in experiments are conceivably related to the presence of TBs, as they are not typically observed in single-crystalline nanowires. But effects of the TBs on hardening are not apparent from our experimental results alone. Hence we performed MD simulations to investigate the atomistic mechanisms controlling the size-dependent strain

Table 1. Fitting Parameters for the Experimental Stress–Strain Data Based on Equation 1

diameter (nm)	n	H (GPa)	E (GPa)
38	0.14	8.89	169
42	0.16	3.85	160
55	0.15	4.24	125
96	0.19	4.05	105
130	0.23	2.44	96

hardening behavior in the five-fold twinned AgNWs. Figure 3 shows the atomic model used in our MD simulations. In Figure 3a, we present the cross-sectional view of a $\langle 110 \rangle$ -oriented AgNW with the characteristic five-fold twinned structure. The angle between two adjacent TBs in any relaxed twin variant T1–T5 is 70.5° . Hence the total angle of combining five relaxed twin variants T1–T5 about the central $[110]$ axis is less than the geometrical total of a regular pentagon by 7.5° .²⁸ This angular mismatch induces an elastic strain in the AgNW core. Figure 3b displays a three-dimensional (3D) view of the atomic structure of the five-fold twinned AgNW, with $\{111\}$ TBs and $\{100\}$ free surfaces.

Figure 4a shows the MD tensile stress–strain curve of a pristine five-fold twinned AgNW with diameter of 6.4 nm. At a strain of about 0.1, the AgNW yields by the nucleation of dislocations from the surface, resulting in an abrupt load drop. The atomic configuration of the AgNW immediately after the load peak is shown in Figure 4b. Each dislocation nucleation site on the surface usually breeds two Shockley partial dislocations of the $(a/6)\langle 112 \rangle$ type (where a denotes the lattice constant). Such symmetric nucleation arises because during tensile loading in the $\langle 110 \rangle$ direction there are two equivalent $\langle 110 \rangle\{111\}$ slip systems that are activated simultaneously, as shown schematically in Figure 4f. After surface nucleation, the Shockley partials glide toward the core of the AgNW as marked in Figure 4b and shown in Figure 4e; they are subsequently blocked by the TBs. This is understandably the unit dislocation process that contributes to the macroscopic hardening of the AgNW. As the applied load increases, the obstructed Shockley partial can transmit across the TB into the adjacent twin variant, leaving a sessile dislocation at the TB as circled in Figure 4c. These

nucleation–transmission events of partial dislocations are repeated during continued deformation, producing a chain of 3D stacking defects, each of which extends across five twin variants centered around the nanowire axis, as shown in Figure 4d.

The above MD results reveal the mechanism of TB-mediated hardening in the five-fold twinned AgNW. However, the corresponding stress–strain curve in Figure 4a does not capture the strain hardening response as measured in our experiments (Figure 2c). This discrepancy reflects a common shortcoming of the MD simulations in producing stress–strain curves when the model nanowire is pristine and free of defects. The absence of the pre-existing defects results in a very high yield stress, which is followed by a sharp load drop (Figure 4a) due to spatially uniform nucleation of many dislocations nearly at the same time. Moreover, the high stress at yielding tends to drive the dislocations to transmit across the TB without contributing much to hardening. Hence the MD results in Figure 4 as well as in past works^{25–27} are representative of the whisker-like behavior,¹ instead of the hardening of five-fold twinned AgNWs as measured in experiments.

Strain Hardening and Size Effect. In order to study the hardening behavior by MD, we introduced pre-existing defects in the simulated five-fold twinned AgNWs. This was achieved by preloading the AgNW plastically and then unloading it to zero stress. During unloading, the majority of dislocations in the five twin variants are annihilated at free surfaces, creating surface defects such as steps, while a few of them are retained as internal defects such as stacking faults within the nanowire bulk and steps at the TBs. The strain at unloading was kept the same for AgNWs of various diameters in order to produce comparable densities of defects. In the experimental samples, surface defects such as steps commonly exist as evidenced by the atomically rough surface in Figure 2b, while internal defects such as stacking faults and TB steps also exist as shown in Figure 2a. Those surface and internal defects understandably have lower activation stresses of dislocation nucleation than the pristine part of the nanowire.⁷ In other words, pre-existing surface and internal defects break the axial symmetry of the “pristine” five-fold twinned AgNW by introducing a statistical distribution to the source strengths of dislocations, which can arise due to different orientations and spacings of steps. Such

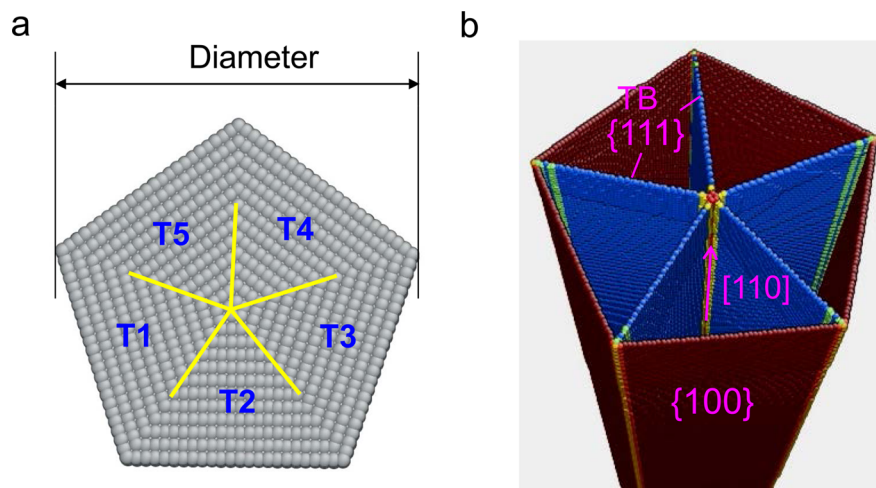


Figure 3. Atomic structure of the five-fold twinned Ag NW. (a) Cross-sectional view, showing twin variants of T1 to T5. (b) Perspective view depicting the $[110]$ -oriented NW containing $\{111\}$ twin boundaries (TBs) and $\{100\}$ free surfaces.

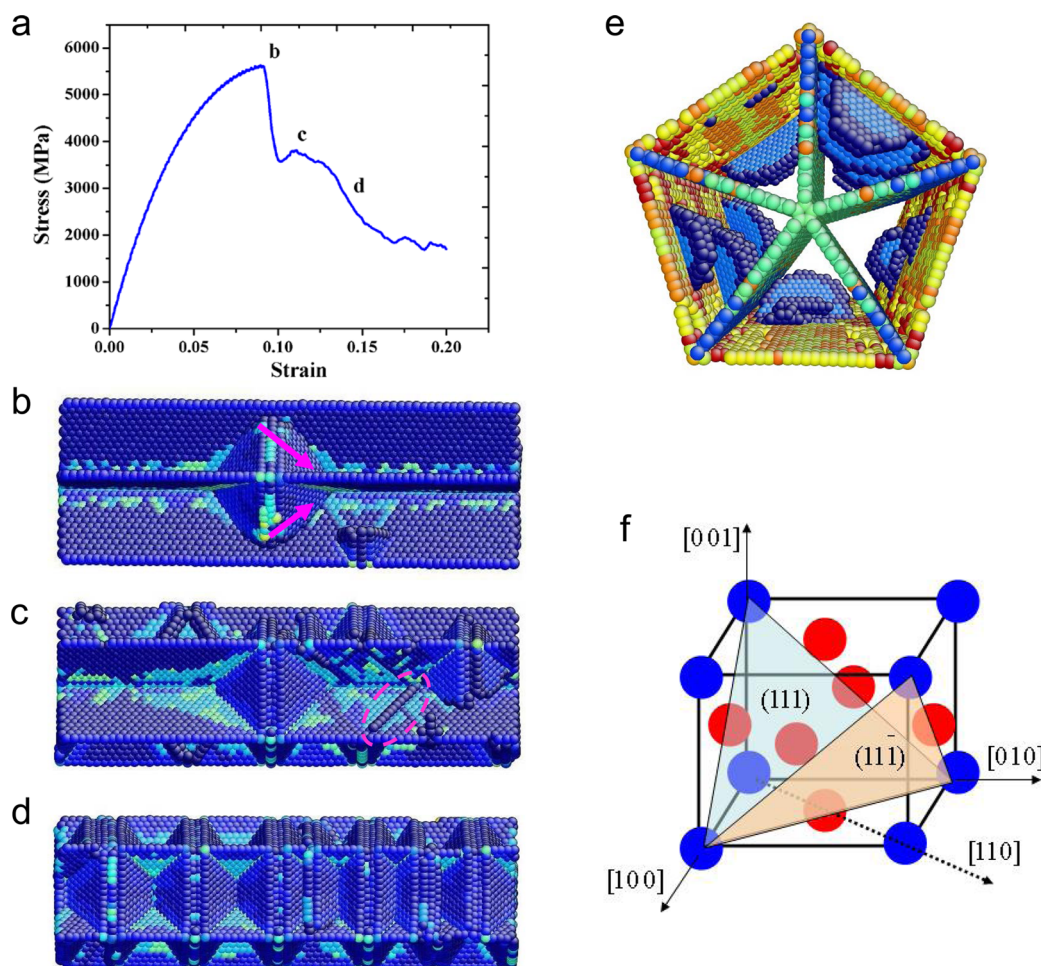


Figure 4. MD simulation results for the pristine Ag NW. (a) Stress–strain curve. (b–d) Atomic configurations of the points b, c, and d as marked in the stress–strain curve in (a). (e) Cross-sectional view of the nanowire showing the dislocation nucleation in two equivalent $[110]\{111}$ slip systems. (f) Schematic of the fcc unit cell showing the activation of the two equivalent $[110]\{111}$ slip systems (shaded triangles) for tensile loading along $[110]$ direction.

symmetry breaking in the “defective” AgNW promotes sequential, spatially nonuniform dislocation nucleation under loading,³⁴ as opposed to collective, uniform nucleation in the pristine AgNW. For a given diameter, the density of pre-existing defects in MD could be controlled by unloading at various strain levels during the postyield deformation.

Figure 5a shows the tensile stress–strain curves from MD simulations for the defective AgNWs of diameters 10.8 and 15 nm, respectively. Table 2 lists the fitting parameters of E , H , and n based on eq 1 for the MD stress–strain data; the associated fitting stress–strain curves are plotted in Figure 5a. The size dependence of E , H , and n is consistent between the experimental and MD results, while the quantitative differences in n and E between experiment and MD can be respectively attributed to the much higher strain rates in MD and the approximate nature of the interatomic potential for Ag. We note that both AgNWs in MD simulations exhibit the hardening behaviors, consistent with the experimental observations (Figure 2c). Significant hardening in defective AgNWs contrasts with the negligible hardening in the pristine five-fold twinned AgNWs in Figure 4a, thus demonstrating the important effect of statistical variation of source strengths of surface dislocations. In contrast, our MD simulations show very limited hardening in prestrained single-crystalline AgNWs with

pre-existing defects (see Figure S1 in Supporting Information); in this case the nucleated dislocations are easily annihilated at the surface due to the lack of stable hardening obstacles. This comparison confirms the unique role of the vertical TBs in the macroscopic hardening of the five-fold twinned AgNW.

To further understand the atomistic mechanisms underlying the macroscopic hardening in the defective five-fold twinned AgNWs, Figure 5b–e shows the side sectional view of the 10.8 nm diameter AgNW at various strain levels, as marked in Figure 5a. Clearly, the zero stress state (Figure 5b) contains a number of pre-existing defects both on the surface and in the bulk unlike the pristine five-fold twinned AgNW in Figure 4b. The initial nonlinear stress–strain response is primarily governed by dislocation nucleation at the surface steps with relatively low activation stresses. Figure 5c shows the surface-nucleated dislocations inside the deformed AgNW. However, the rate of surface nucleation and the resultant rate of stress relaxation are still relatively low. Moreover, the nucleated dislocations are mostly blocked by TBs, resulting in the back stresses to resist against the continued operation of surface dislocation sources. As a result, the pronounced strain hardening ensues. When the tensile load increases to around point d in Figure 5a, the rate of surface dislocation nucleation becomes high and the TB-obstructed dislocations can often cross-slip into adjacent twin

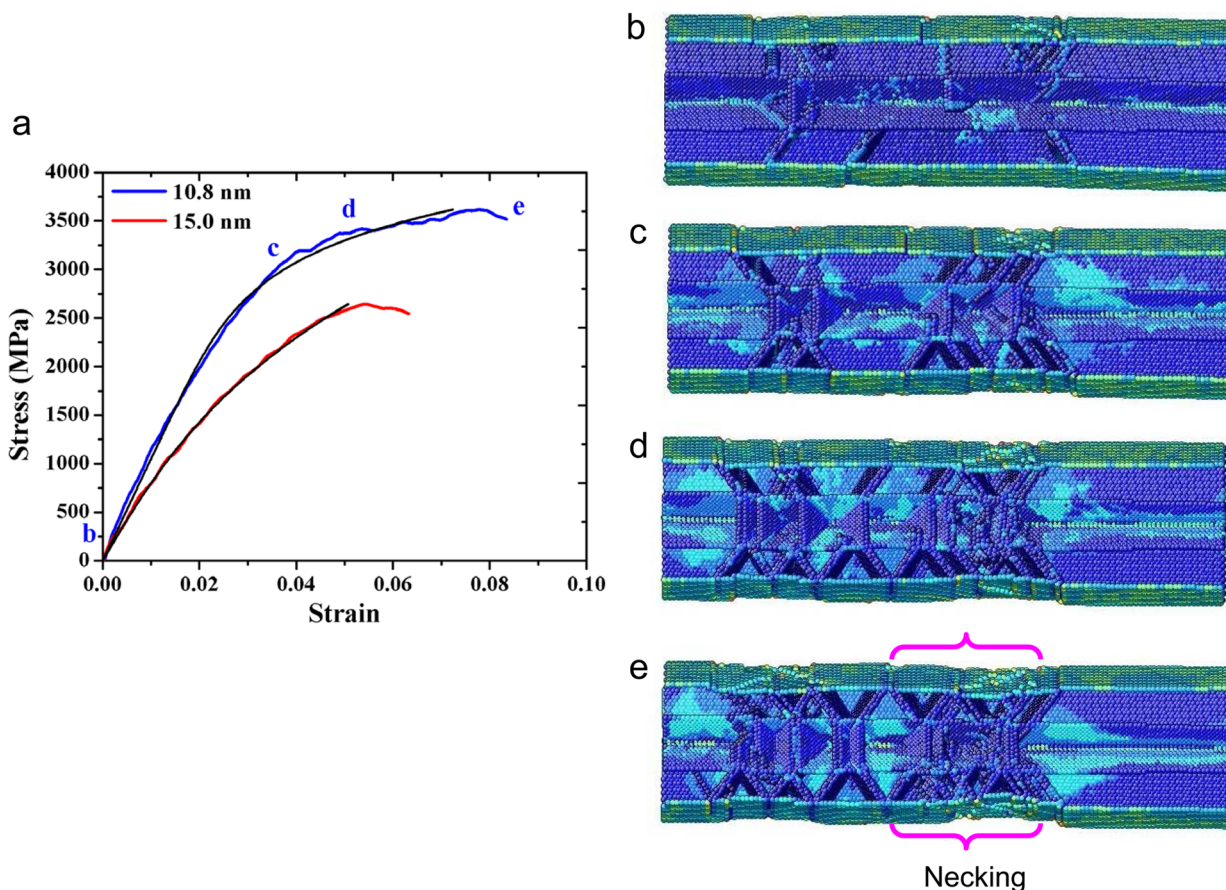


Figure 5. Size-dependent hardening behavior from MD simulations. (a) Stress–strain curves for the tensile loading of defective five-fold twinned Ag NWs of 10.8 and 15 nm in diameter, respectively. The red and blue curves are the MD data, while the black curves are the Ramberg–Osgood fitting based on eq 1. (b–e) Atomic configurations of the 10.8 nm diameter NW at various strain levels as marked in (a). The onset of necking is marked by pink brackets in (e).

Table 2. Fitting Parameters for the MD Stress–Strain Data Based on Equation 1

diameter (nm)	n	H (GPa)	E (GPa)
10.8	0.12	5.32	105
15	0.27	6.70	85

variants (Figure 5d), so that the hardening rate (i.e., the slope of the stress–strain curve) is reduced. At point e, the dislocation activity starts to be confined into a narrow portion of the AgNW that subsequently leads to necking and ductile failure, as marked in Figure 5e.

The simulated stress–strain curves in Figure 5a also capture the size/diameter dependent strength and hardening in five-fold twinned AgNWs, consistent with the experimental results in Figure 2c. Namely, thinner AgNWs achieve higher strength and more hardening that leads to higher tensile ductility. Since TBs in the five-fold twinned AgNW play a similar role of obstructing dislocations as grain boundaries in bulk polycrystalline metals, the size-dependent strength in AgNWs can be attributed to the characteristic smaller-is-stronger size effect in the nanoscale. Specifically, as the diameter of the AgNW decreases, the effective distance between the surface dislocation source and the TB decreases. Such size reduction can lead to strong interactions between the TBs and surface dislocation sources, which are facilitated by the back stresses generated by the TB-obstructed dislocations. Hence, the higher strength in

the smaller AgNW can be attributed to the relatively high stresses required to sustain the operation of surface dislocation sources, which is also responsible for the high hardening rate in the smaller AgNW. The high hardening rate can delay the onset of necking, thereby promoting the tensile ductility,⁴ which is consistent with both the experimental and MD results.

Necking and Fracture. The final stage of tensile deformation of five-fold twinned AgNWs involved the onset and growth of necks. Such localized deformation eventually concentrated to one neck, leading to the fracture of the AgNW. Figure 6 shows the necking behavior of two AgNWs with the respective initial diameters of 6.4 and 10.8 nm, close to their failure point. Both AgNWs are 34.7 nm long. Interestingly, the smaller wire in Figure 6a exhibits several local necks along its length, while the larger wire in Figure 6b,c exhibits only a single neck. The development of multiple necks in the smaller wire indicates that the growth of the neck can become difficult owing to the local hardening induced by the TBs. Consequently, the plastic deformation tends to be delocalized, resulting in multiple necks. Such multiple-necking mode in five-fold twinned AgNWs has been observed by Filletier et al.²⁵ in experiments. They measured the number and the length of the necks (which they referred to as “plastic zones”) as a function of the AgNW diameter and found that the number of necks decreased and the length of the neck increased with increasing nanowire diameter. Our MD results lend a direct proof for the size-dependent multiple necking behavior.

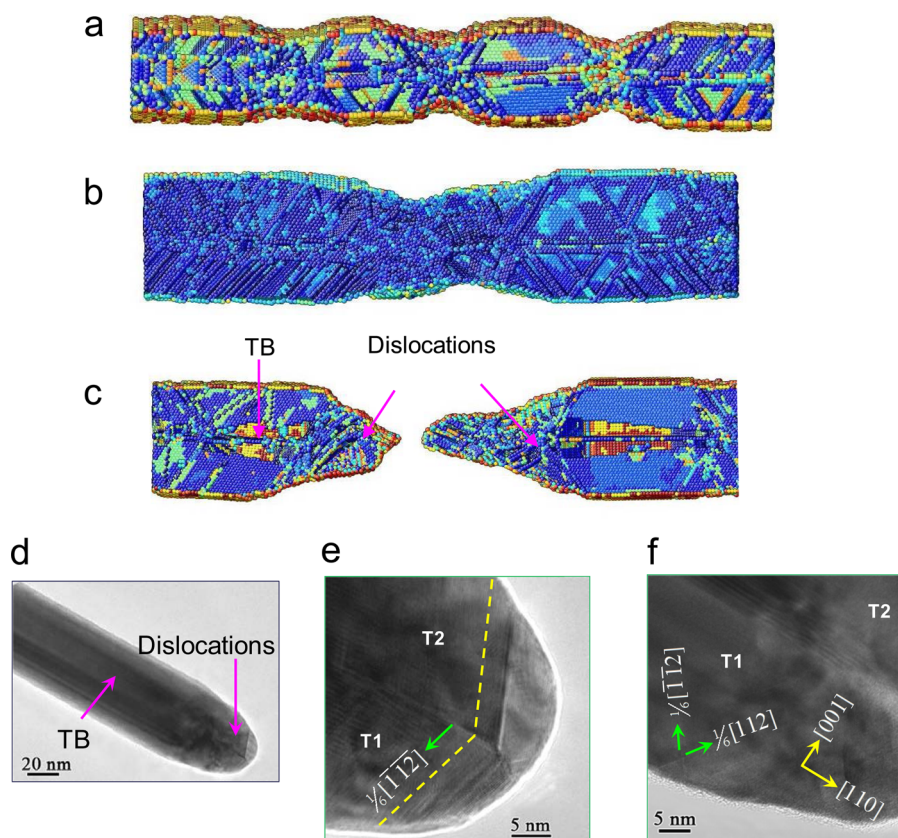


Figure 6. Deformation via multiple necking and ductile failure. (a) A MD snapshot showing the formation of multiple necks in a deformed AgNW with initial diameter of 6.4 nm. MD snapshots are also shown for (b) the formation of a single neck in a deformed AgNW with initial diameter of 10.8 nm and (d) subsequent fracture in the necked region with a high density of dislocations. (d) TEM image of dislocations near the fracture region. (e) TEM image showing the cross slip of the Shockley partial across the TB. (f) TEM image showing dislocation activity in the two equivalent $[110]\{111\}$ slip systems.

As mentioned earlier, the AgNW failed by necking at one of the necks in both the experiment and MD. Figure 6d shows the post-mortem TEM image of the failure region. The rounded fracture surface is characteristic of the ductile rupture resulting from the dislocation shear-induced thinning of the AgNW. This is in contrast to the flat brittle-like fracture surface reported by Filletter et al.²⁵ Figure 6e shows that a high density of dislocations can be seen near the fracture surface, while the portions of the nanowire away from the fracture surface have a lower dislocation density. This is consistent with our MD result as shown in Figure 6c. High-resolution TEM imaging of the failure surface also revealed direct evidence for the cross-slip of the Shockley partials at the TB (Figure 6e), as observed in our MD simulations (Figure 4b–d). Figure 6f shows the slip activity in the two equivalent $[110]\{111\}$ slip systems, as revealed by MD in Figure 4e,f. These results demonstrate the direct correlation between our experimental and MD results.

Role of Pre-existing Defects. Recall that our MD results in Figure 5a depicting hardening were obtained for defective five-fold twinned AgNWs, while the MD results in Figure 4a shows that pristine AgNWs did not exhibit hardening. Such a difference indicates that plastic deformation in AgNW is strongly dependent on the density of pre-existing defects such as surface steps. The critical role of pre-existing defects on the plasticity of nanostructures have previously been underscored in the studies of deformation of prestrained Au nanopillars,³⁵ single-crystalline Au nanowhiskers¹⁴ and Cu nanowires.⁹ Essentially, the strain hardening behavior in the deformation

experiment at a fixed loading rate is controlled by the interplay between the elastic strain rate (tends to increase the stress) and the plastic strain rate (tends to lower the stress), the latter of which is dictated by the dislocation nucleation rate in small-volume materials.^{7,34}

In order to understand the hardening behavior of the AgNW as a function of the density of the pre-existing defects, we simulated three samples (diameter of 10.8 nm) with different initial pre-existing defect densities of surface steps, as shown in Figure S2 (Supporting Information). The desired defect densities ρ were achieved by varying the strain level at which the nanowire was unloaded. The tensile stress–strain curves for these three AgNWs are compared in Figure S2a of Supporting Information with the corresponding side sectional views of the initial states shown in Supporting Information Figure S2b–d. The stress–strain curves show that the AgNW with the smaller defect density (Supporting Information Figure S2b) hardens more and achieves higher ultimate tensile strength than the other two AgNWs with higher defect densities (Supporting Information Figure S2c,d). The AgNW with the least defect density produces the least amount of surface dislocations to plastically relax the system. As a result, the stress in this AgNW is the largest, when the same tensile strain is attained in three AgNWs. This result underscores the critical role of pre-existing defect density in influencing the hardening behavior and the ultimate tensile strength of the five-fold twinned AgNW.

Finally, we comment on the difference in the amount of remnant dislocations after unloading between the recent

experimental reports^{30,31} and the present MD simulations, which is primarily caused by the different tensile strains applied before unloading. In the strain recovery experiments,^{30,31} the applied strains were small, typically less than 2–3%. In contrast, our MD simulations allow the strain-controlled loading and the nanowires are not very long, such that large strains up to ~10% can be applied without necking instability. As a result, there are more dislocations nucleated during loading and accordingly more remnant dislocations after unloading. It should be noted that due to the high strain rate in MD ($\sim 10^7$ s⁻¹ to 10^9 s⁻¹), more remnant dislocations are needed to act as pre-existing defects during subsequent loading in order to bring out the pronounced strain hardening behavior. In contrast, less pre-existing defects usually exist in real samples. But the low loading rates ($\sim 10^{-1}$ /s or 1.5×10^{-3} /s) in the experiments give the nanowire more time to nucleate the sufficient amount of dislocations necessary for the measurable strain hardening response.

Conclusion. We have studied the unique strain hardening behavior of five-fold twinned AgNWs using a combined experimental and computational approach. Both our experiments and MD stimulations showed the strain hardening in five-fold twinned AgNWs, not exhibited by single-crystalline nanowires or other nanostructures. Smaller wires hardened significantly and achieved higher ultimate tensile strength than the larger ones. Such hardening response and size effect were shown to be caused by the effective obstruction of surface nucleated dislocations by TBs. Our MD simulations further revealed the important role of the statistical variation of source strengths of surface-nucleated dislocations in the small-sized nanostructures. Overall, this work reveals the mechanistic underpinnings of strain hardening in metallic nanostructures by coherent TBs and points to possible routes of enhancing the tensile ductility by engineering the internal interfaces and defects.

Methods. Experiment. Tensile tests were performed using an in situ SEM nanomechanical testing up at the strain rate of $\sim 10^{-1}$ /s.³⁶ An individual NW was clamped on a nanomanipulator tip and an atomic force microscopy (AFM) cantilever using electron beam induced deposition of carbonaceous materials in the SEM. The force was applied using the nanomanipulator (Klocke Nanotechnik, Germany) on one side of the freestanding NW and was measured on the other side using the AFM cantilever. A series of SEM images were taken during the tension tests; the NW strain was measured by digital image correlation of the SEM images. Pentagonal cross-section was used in calculating the stress.

Modeling. MD simulations were performed using LAMMPS.³⁷ We employed a recent embedded atom method (EAM) potential of Ag developed by Williams et al.³⁸ Stacking faults, twin boundaries, and surfaces are visualized by coloring the atoms based on their centro-symmetry parameters.³⁹ Tensile tests were conducted on the model AgNWs at 10 K and a strain rate ranging from 10^7 to 10^9 s⁻¹. Periodic boundary conditions were applied along the [110] axial direction and the lateral free surfaces were fully relaxed.

■ ASSOCIATED CONTENT

■ Supporting Information

Additional supporting figures are provided. The Supporting Information is available free of charge on the ACS Publications website at DOI: 10.1021/acs.nanolett.5b01015.

■ AUTHOR INFORMATION

Corresponding Authors

*E-mail: ting.zhu@me.gatech.edu (T.Z.).

*E-mail: yong_zhu@ncsu.edu (Y.Z.).

Notes

The authors declare no competing financial interest.

■ ACKNOWLEDGMENTS

We acknowledge the support by the NSF Grants DMR-1410331 and DMR-1410475.

■ REFERENCES

- (1) Brenner, S. S. *J. Appl. Phys.* **1956**, *27* (12), 1484–1491.
- (2) Uchic, M. D.; Dimiduk, D. M.; Florando, J. N.; Nix, W. D. *Science* **2004**, *305* (5686), 986–989.
- (3) Greer, J. R.; Nix, W. D. *Phys. Rev. B* **2006**, *73* (24), 245410.
- (4) Zhu, T.; Li, J. *Prog. Mater. Sci.* **2010**, *55* (7), 710–757.
- (5) Greer, J. R.; De Hosson, J. T. M. *Prog. Mater. Sci.* **2011**, *56* (6), 654–724.
- (6) Park, H. S.; Gall, K.; Zimmerman, J. A. *J. Mech. Phys. Solids* **2006**, *54* (9), 1862–1881.
- (7) Zhu, T.; Li, J.; Samanta, A.; Leach, A.; Gall, K. *Phys. Rev. Lett.* **2008**, *100*, 025502.
- (8) Kiener, D.; Minor, A. M. *Nano Lett.* **2011**, *11* (9), 3816–3820.
- (9) Peng, C.; Zhan, Y.; Lou, J. *Small* **2012**, *8* (12), 1889–1894.
- (10) Peng, C.; Zhong, Y.; Lu, Y.; Narayanan, S.; Zhu, T.; Lou, J. *Appl. Phys. Lett.* **2013**, *102* (8), 083102.
- (11) Wang, J. W.; Narayanan, S.; Huang, J. Y.; Zhang, Z.; Zhu, T.; Mao, S. X. *Nat. Commun.* **2013**, *4*, 2340.
- (12) Liang, W. W.; Zhou, M.; Ke, F. J. *Nano Lett.* **2005**, *5* (10), 2039–2043.
- (13) Seo, J. H.; Yoo, Y.; Park, N. Y.; Yoon, S. W.; Lee, H.; Han, S.; Lee, S. W.; Seong, T. Y.; Lee, S. C.; Lee, K. B.; Cha, P. R.; Park, H. S.; Kim, B.; Ahn, J. P. *Nano Lett.* **2011**, *11* (8), 3499–3502.
- (14) Sedlmayr, A.; Bitzek, E.; Gianola, D. S.; Richter, G.; Moenig, R.; Kraft, O. *Acta Mater.* **2012**, *60* (9), 3985–3993.
- (15) Wang, L.; Liu, P.; Guan, P.; Yang, M.; Sun, J.; Cheng, Y.; Hirata, A.; Zhang, Z.; Ma, E.; Chen, M.; Han, X. *Nat. Commun.* **2013**, *4*, 2413.
- (16) Wang, J.; Zeng, Z.; Weinberger, C. R.; Zhang, Z.; Zhu, T.; Mao, S. X. *Nat. Mater.* **2015**, DOI: 10.1038/nmat4228.
- (17) Li, X.; Wei, Y.; Lu, L.; Lu, K.; Gao, H. *Nature* **2010**, *464* (7290), 877–880.
- (18) Zhu, T.; Gao, H. *J. Scr. Mater.* **2012**, *66* (11), 843–848.
- (19) Deng, C.; Sansoz, F. *Nano Lett.* **2009**, *9* (4), 1517–1522.
- (20) Wang, J.; Sansoz, F.; Huang, J.; Liu, Y.; Sun, S.; Zhang, Z.; Mao, S. X. *Nat. Commun.* **2013**, *4*, 1742.
- (21) Lu, L.; Chen, X.; Huang, X.; Lu, K. *Science* **2009**, *323* (5914), 607–610.
- (22) Jang, D. C.; Li, X. Y.; Gao, H. J.; Greer, J. R. *Nat. Nanotechnol.* **2012**, *7* (9), 594–601.
- (23) Zhou, H.; Li, X.; Qu, S.; Yang, W.; Gao, H. *Nano Lett.* **2014**, *14* (9), 5075–5080.
- (24) Zhu, Y.; Qin, Q. Q.; Xu, F.; Fan, F. R.; Ding, Y.; Zhang, T.; Wiley, B. J.; Wang, Z. L. *Phys. Rev. B* **2012**, *85* (4), 045443.
- (25) Filleter, T.; Ryu, S.; Kang, K.; Yin, J.; Bernal, R. A.; Sohn, K.; Li, S. Y.; Huang, J. X.; Cai, W.; Espinosa, H. D. *Small* **2012**, *8* (19), 2986–2993.
- (26) Cao, A. J.; Wei, Y. G. *Phys. Rev. B* **2006**, *74* (21), 214108.
- (27) Leach, A. M.; McDowell, M.; Gall, K. *Adv. Funct. Mater.* **2007**, *17* (1), 43–53.
- (28) Monk, J.; Hoyt, J. J.; Farkas, D. *Phys. Rev. B* **2008**, *78* (2), 024112.
- (29) Lucas, M.; Leach, A. M.; McDowell, M. T.; Hunyadi, S. E.; Gall, K.; Murphy, C. J.; Riedo, E. *Phys. Rev. B* **2008**, *77* (24), 245420.
- (30) Bernal, R. A.; Aghaei, A.; Lee, S.; Ryu, S.; Sohn, K.; Huang, J.; Cai, W.; Espinosa, H. *Nano Lett.* **2015**, *15* (1), 139–146.

- (31) Qin, Q.; Yin, S.; Cheng, G.; Li, X.; Chang, T.-H.; Richter, G.; Zhu, Y.; Gao, H. *Nat. Commun.* **2015**, *6*, 5983.
- (32) Sun, Y. G.; Gates, B.; Mayers, B.; Xia, Y. N. *Nano Lett.* **2002**, *2* (2), 165–168.
- (33) Wiley, B.; Sun, Y. G.; Xia, Y. N. *Acc. Chem. Res.* **2007**, *40* (10), 1067–1076.
- (34) Argon, A. S. *Philos. Mag.* **2013**, *93* (28–30), 3795–3808.
- (35) Lee, S.-W.; Han, S. M.; Nix, W. D. *Acta Mater.* **2009**, *57* (15), 4404–4415.
- (36) Zhu, Y.; Xu, F.; Qin, Q. Q.; Fung, W. Y.; Lu, W. *Nano Lett.* **2009**, *9* (11), 3934–3939.
- (37) Plimpton, S. J. *Comput. Phys.* **1995**, *117* (1), 1–19.
- (38) Williams, P. L.; Mishin, Y.; Hamilton, J. C. *Modell. Simul. Mater. Sci. Eng.* **2006**, *14* (5), 817–833.
- (39) Li, J. *Modell. Simul. Mater. Sci. Eng.* **2003**, *11* (2), 173–177.